

Strength, Deformability and X-ray Micro-CT Observations of Deeply Buried Marble Under Different Confining Pressures

Sheng-Qi Yang¹ · Yang Ju¹ · Feng Gao¹ · Yi-Lin Gui²

Received: 16 November 2015 / Accepted: 23 June 2016 / Published online: 2 July 2016
© Springer-Verlag Wien 2016

Abstract In this research, a series of triaxial compression experiments and X-ray observations were conducted to explore the strength, deformability and internal damage mechanism of deeply buried marble. The results show that an increase in confining pressure results in obvious brittle–ductile transition characteristics of deeply buried marble. The Young’s modulus of the marble increased nonlinearly with increasing confining pressure. The peak and residual strength of the marble exhibit a clear linear relationship with the confining pressure, which can be described by the linear Mohr–Coulomb criterion. The sensitivity of the residual strength on the confining pressure was clearly higher than that of the peak strength. After uniaxial and triaxial compression failure, marble specimens were analyzed using a three-dimensional X-ray micro-CT scanning system. Based on horizontal and vertical cross-sections, the marble specimen is mainly dominated by axial splitting tensile cracks under uniaxial compression, but under confining pressure, the marble specimen is mainly dominated by a single shear crack. To quantitatively evaluate the internal damage of the marble material, the crack area and aperture extent for each horizontal cross-section were calculated by analyzing the binarized pictures. The system of crack planes under uniaxial compression is more complicated than that under triaxial compression, which is also

supported by the evolution of the crack area and aperture extent. Finally, the brittle–ductile transition mechanism of the marble is discussed and interpreted according to the proposed conceptual models.

Keywords Deeply buried marble · Strength · Brittle–ductile transition · X-ray micro-CT · Crack

1 Introduction

The Jinping II Hydropower Project is located in the upriver of the Yalong River in Sichuan Province, southwestern China. As described by Wu et al. (2010) and Feng et al. (2015), Jinping II mainly consists of three auxiliary tunnels and a sluice dam on the western side of the Jinping Mountain, four headrace tunnels through the mountain and an underground powerhouse complex on the eastern side of the mountain (Fig. 1). The total installed capacity is 4800 MW. Four headrace tunnels with a diameter of 12–13 m and a total length of 16.67 km are constructed at depths of 1500–2000 m, and the maximum buried depth is up to 2525 m. The average principal stress of the rock mass ranges from 35 to 50 MPa, and the maximum vertical principal stress is as high as 60 MPa, according to the measured geostress data and back analysis of the geostress field (Jiang et al. 2010). The main stratum excavated for the underground tunnels is Triassic marble. The uniaxial compressive strength of the marble in the project region ranges from 80 to 120 MPa (Li et al. 2012a, b), which indicates that it is a medium to hard rock material. Therefore, the experimental studies of the strength, deformability and failure behavior of the marble under higher geostress conditions are significant to understand the

✉ Sheng-Qi Yang
yangsqi@hotmail.com

¹ State Key Laboratory for Geomechanics and Deep Underground Engineering, School of Mechanics and Civil Engineering, China University of Mining and Technology, Xuzhou 221116, People’s Republic of China

² Nanyang Centre for Underground Space, School of Civil and Environmental Engineering, Nanyang Technological University, Singapore 639798, Singapore

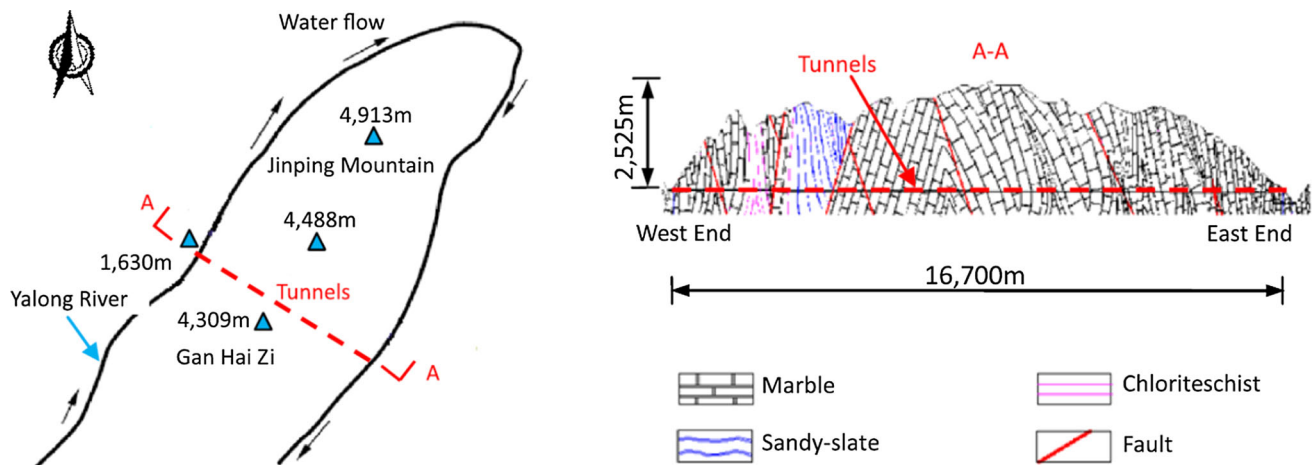


Fig. 1 Deeply buried tunnels of the Jinping II Hydropower Station, China (Feng et al. 2015)

stability of the Jinping II Hydropower Project (Aliha 2014; Yang et al. 2015a).

Li et al. (2013) conducted conventional triaxial compression and reducing confining pressure tests for marble specimens and analyzed the influence of two loading paths on the mechanical behavior of the marble. The experimental results show that in the loading and unloading test, peak strength, lateral strain, axial strain and plastic deformation increase significantly as the confining pressure increases. The fracture mode is mainly a single shear fracture for the triaxial compression test and post-peak test, and the angle between the failure surface and the ends of the rock material becomes smaller with the increase in confining pressure. By conducting triaxial compression loading–unloading tests for marble specimens under different confining pressures and unloading rates, Huang and Li (2014) found that the magnitude of the initial confining pressure and unloading rate significantly influenced the rock failure modes and strain energy conversion (accumulation, dissipation and release) during unloading. Yang et al. (2008) completed conventional triaxial compression experiments on flawed marble specimens. The results show that the peak strength and failure mode of the marble depend not only on the geometry of the flaw, but also on the confining pressure. By proposing a new incrementally cyclic loading–unloading pressure test method, Qiu et al. (2014) experimentally analyzed the pre-peak unloading damage evolution characteristics of the marble from the Jinping II Hydropower Project. The results demonstrated that the pre-peak damage and deformation characteristics of marble specimens could be easily quantified by the irreversible strains.

Rock masses commonly have a large number of cracks and flaws (Yang et al. 2009), and investigating their integrity and load bearing capacity via the frame work of

fracture mechanics may provide more reliable predictions under real situations (Ayatollahi and Aliha 2007; Aliha et al. 2012, 2013; Funatsu et al. 2014). Next, we briefly describe fracture mechanics and their abilities to accommodate the cracked and flawed rock masses and structures. Ayatollahi and Aliha (2007) proposed a modified maximum tangential stress (MTS) criterion to predict the mixed mode I (crack opening mode) and II (crack sliding mode) fracture toughness data on the basis of the experimental results of semi-disk brittle rock specimens. Akbardoost and Ayatollahi (2014) completed the experiments on the mixed mode fracture behavior of marble using a center cracked circular disk (CCCD) specimen and an edge cracked triangular (ECT) specimen. Then, they proposed a modified MTS criterion to predict the mixed mode fracture resistance of marble obtained from the ECT specimens only using the mode I fracture resistance measured from a CCCD specimen. Based on the experimental results of the fracture toughness of marble under mixed mode conditions, Chang et al. (2002) analyzed the size effects in terms of the specimen thickness, diameter and notch length on the fracture toughness of marble. By taking into account the geometry and loading conditions of the tested specimen, Aliha et al. (2012, 2013) put forward generalized maximum tangential stress (GMTS) criterion, which is in a good agreement with the experimental results of the Brazilian disk (BD), the semicircular bend (SCB) and ECT marble specimens.

However, previous experimental studies of the strength and deformation failure behavior of marble using X-ray computer tomography (CT) observations have rarely considered triaxial tests. Generally, X-ray CT is the best noninvasive nondestructive method to characterize complex pore structures and has been applied to explore the internal damage behavior of some rock materials (Ge et al.

2001; Hirono et al. 2003, 2008; Feng et al. 2004; Sufian and Russell 2013; Zhao et al. 2014; Meier et al. 2014; Yang et al. 2015b). Therefore, in this paper, we report the results of a series of uniaxial and conventional triaxial compression tests on deeply buried marble under different confining pressures ranging from 0 to 50 MPa. Based on the experimental results, we first investigate the influence of the confining pressure on the strength and deformation parameters of marble. Then, using an X-ray micro-CT scanning system, the internal damage characteristics of the deformed marble specimens are analyzed in detail.

2 Marble Material and Testing Procedure

Marble, located in the number 3[#] test branch tunnel of an auxiliary cave in the Jinping II Hydropower Project, was chosen for testing. This marble is buried at a depth of approximately 2270 m. According to X-ray diffraction (XRD) (Fig. 2), the marble material mainly consists of carbonate minerals (calcite), with small quantities of quartz and amorphous solids. The marble has a crystalline and blocky structure (Fig. 2), that is macroscopically very homogeneous with a connected porosity of 1.09 % and an average density of approximately 2710 kg/m³.

In accordance with the method suggested by the ISRM (Fairhurst and Hudson 1999), the length-to-diameter ratio of the tested specimens should be between 2.0 and 3.0 to minimize the influence of the end friction effects on the results and to ensure a uniform stress state within the specimen. Therefore, all of the tested marble specimens are cylindrical, 50 mm in diameter and 100 mm long. The mechanical behaviors of specimens under triaxial compression were determined following the method suggested by the ISRM (Fairhurst and Hudson 1999).

The experiments were conducted on servo-controlled triaxial equipment, which can be used to perform hydrostatic pressure tests, conventional triaxial compression tests under drained or undrained conditions, triaxial seepage

tests, triaxial creep tests and chemical corrosion tests. When testing, the axial displacement is measured with two linear variable differential transformers (LVDTs), which are fixed between the bottom and top surfaces of the specimen inside the triaxial cell. The triaxial compression experiment had the following steps: The confining pressure was first applied to a desired value at a constant rate of 0.5 MPa/s, which ensured that the specimen was under uniform hydrostatic stress. The deviatoric stress was then loaded on the top surface of the specimen at a constant axial stress rate of 0.127 MPa/s until failure occurred. A total of eight specimens have been tested with confining pressures ranging from 0 to 50 MPa, and a total of ten specimens were carried out by the indirect Brazilian test. All marble specimens that were in the indirect Brazilian test were cylindrical, 50 mm in diameter and 25 mm thickness.

3 Strength and Deformability

Figure 3 presents the axial stress–axial strain curve and ultimate failure mode of marble under uniaxial compression. From Fig. 3, the uniaxial compressive strength (UCS) of marble specimen A4[#] is 99.11 MPa and the UCS of specimen A3[#] is 96.37 MPa. Furthermore under uniaxial compression, two marble specimens have a consistent deformation behavior before peak strength, but marble specimen A4[#] shows more brittleness than A3[#] after peak strength. However, from the ultimate failure mode, the marble specimens have noticeable axial splitting tensile cracks, which validate the obviously brittle failure of the marble material under uniaxial compression.

Figure 4 illustrates the indirect Brazilian tensile strength (σ_t) of ten marble specimens and the corresponding tensile failure modes. From Fig. 4, the tensile strength of the marble specimens ranges from 5.47 to 10.91 MPa, and the average is approximately 8.30 MPa. Thus, we obtain a UCS-to- σ_t ratio of approximately 11.78. The dispersion

Fig. 2 SEM photomicrographs and XRD of the marble in this research

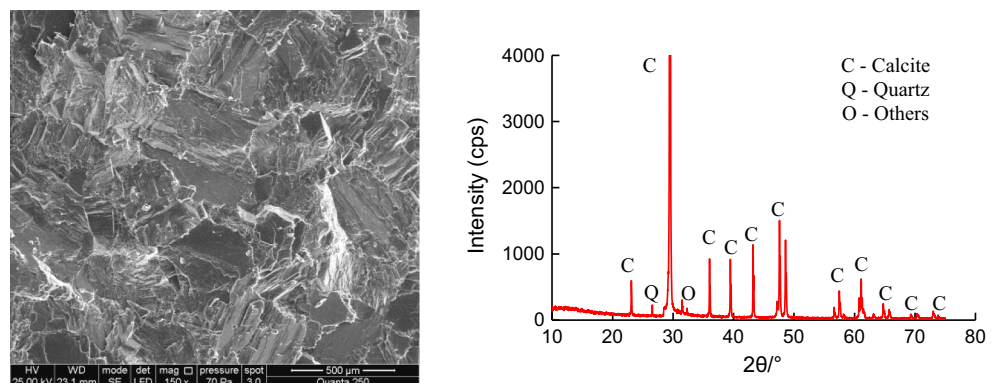


Fig. 3 Uniaxial compression test results of marble

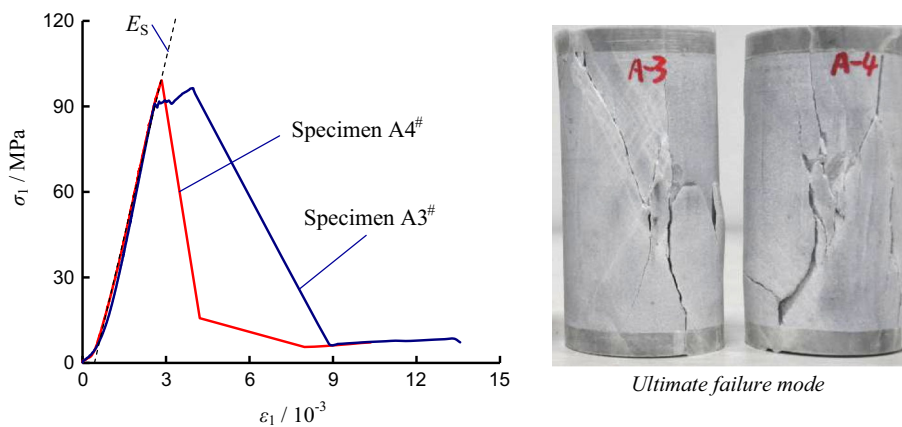
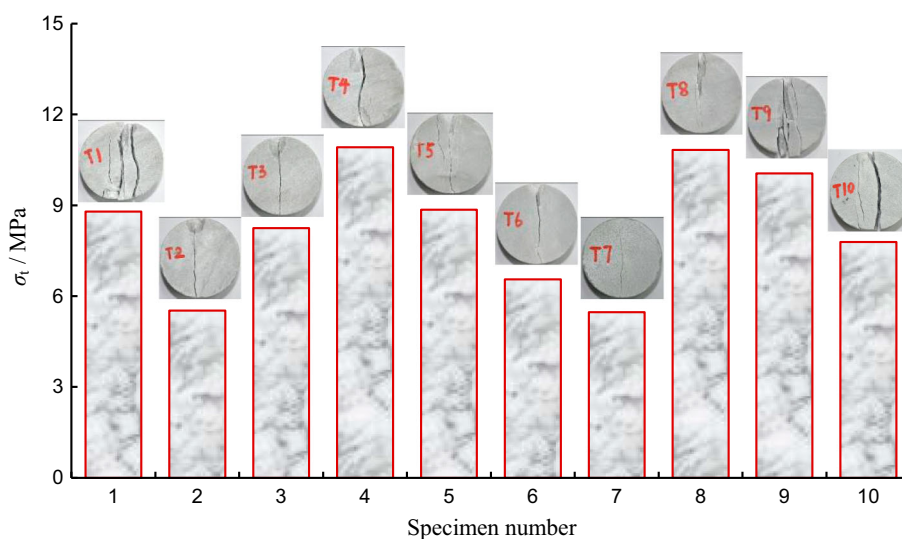


Fig. 4 Indirect Brazilian tensile strength of marble



coefficient (the ratio of the D value between the maximum and the minimum to the average) of the tensile strength of the tested marble is approximately 65.5%. The tensile failure mode of the tested marble is basically entirely the central splitting fracture, and main tensile cracks can be observed in the central region of the marble specimen.

The deviatoric stress–axial strain curves for marble under different confining pressures are presented in Fig. 5, where σ_1 and σ_3 represent the major principal stress and the confining pressure, respectively; ε_1 is the axial strain; and σ_{cr} and σ_p are the residual strength and peak strength, respectively, which are confirmed in accordance with the deviatoric stress–axial strain curves of marble specimens. A typical example at $\sigma_3 = 5$ MPa is shown in Fig. 5. In Fig. 5, the post-peak deformation changes gradually from strain softening to strain hardening with increasing confining pressure. When σ_3 equals ~ 50 MPa, the deformation of the marble specimen has a distinct yielding platform and plastic flow occurs, i.e., the post-peak deformation behavior of the specimen changes into ideal plasticity.

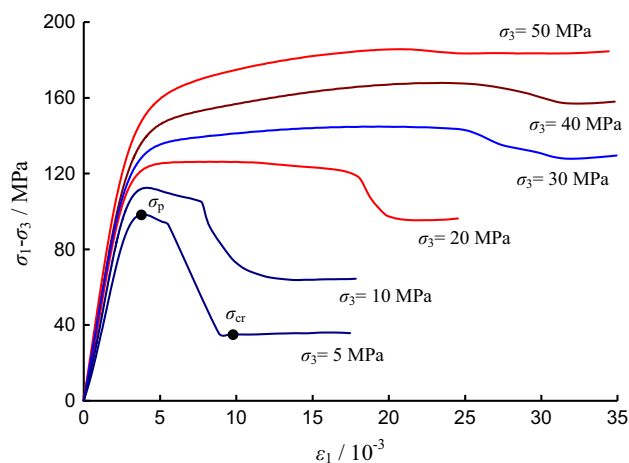


Fig. 5 Deviatoric stress–axial strain curves of marble under different confining pressures

To analyze the influence of the confining pressure on the elastic modulus (E_s) of marble, we used the average slope of the approximately straight line portion of the

deviatoric stress–axial strain curve before the peak strength to calculate E_S , as shown in Fig. 3. However, the deformation modulus (E_{50}) is defined as the slope between the origin and the stress at half of the peak strength. The peak axial strain (ε_{1c}) refers to the strain value reaching the peak strength. Table 1 lists the detailed deformation values of the marble specimens in this study.

Based on the data listed in Table 1, Fig. 6 shows the influence of the confining pressure on the Young's modulus and peak axial strain of marble specimens in the range of tested confining pressures from 0 to 50 MPa. As Fig. 6a illustrates, the Young's modulus increased nonlinearly with increasing confining pressure. It should be noted that the elastic modulus of the marble specimen under uniaxial compression ($\sigma_3 = 0$ MPa) is approximately 45.06 MPa, which is higher than that at $\sigma_3 = 5$ MPa, but the deformation modulus at $\sigma_3 = 0$ MPa is lower than that at $\sigma_3 = 5$ MPa. At $\sigma_3 = 5$ MPa, the elastic modulus and deformation modulus were 36.36 and 32.46 GPa, respectively. When σ_3 was increased to 50 MPa, the elastic modulus and the deformation modulus increased nonlinearly to 53.07 and 51.75 GPa, respectively. Furthermore, the difference between the elastic modulus and the deformation modulus tended to decrease as σ_3 increased, which was the result of the less pronounced stage of micro-crack closure at higher confining pressures. To describe the relationship between the Young's moduli of the marble and confining pressures, a power function is proposed (Fig. 6a). However, from Fig. 6b, an increase in the confining pressure led the peak axial strain of marble to increase greatly as σ_3 increased to 40 MPa, whereas the peak axial strain decreased from 23.45×10^{-3} to 20.64×10^{-3} as σ_3 increased from 40 to 50 MPa.

The Mohr–Coulomb criterion is a common strength criterion, which have been applied widely to rock mechanics and engineering practice. In this section, the Mohr–Coulomb criterion is used to investigate the effect of the confining pressure on the peak strength and residual strength of marble. The linear Mohr–Coulomb criterion can

be expressed with the following equation (Jaeger et al. 2007):

$$\sigma_S = \sigma_0 + q\sigma_3 = \frac{2C \cos \phi + \sigma_3(1 + \sin \phi)}{1 - \sin \phi} \quad (1)$$

where σ_S is the maximum axial supporting capacity of rock; σ_0 is usually regarded as the uniaxial compressive strength (UCS) of rock material; and q is an influence coefficient of confining pressure on the σ_S of rock. The σ_0 and q are related to the cohesion C and the internal friction angle ϕ .

Based on the strength data listed in Table 1, the influence of σ_3 on the peak strength of marble is presented in Fig. 7. The figure indicates that the peak strength of marble has a distinct linear behavior with an increase in σ_3 . Furthermore, the sensitivity of the residual strength on the confining pressure was clearly higher than that for the peak strength. By using the linear Mohr–Coulomb criterion, the peak and residual strength parameters of marble are calculated and listed in Table 2. The peak cohesion of marble is 28.22 MPa, which is considerably higher than the residual cohesion of approximately 3.83 MPa. However, the peak internal friction angle of marble is 28.2° , which is significantly lower than the residual internal friction angle of approximately 39.7° .

4 X-ray Micro-CT Observations

In this study, X-ray computed tomography (CT) scanning of the marble specimen was conducted using a Nanotom 160 high-resolution micro-CT at a spatial resolution of 30 μm . The X-ray beam penetrating the specimen was measured using an array of detectors. The X-rays are produced by electrons striking a Mo-W alloy target in an X-ray tube. The electron current was 90 μA , the accelerating voltage was 130 kV and the scanning time was 4 s. The degree of X-ray attenuation depends on the density and the atomic number of the materials composing the specimens. Materials with a higher density and higher atomic

Table 1 Strength and deformation parameters of marble under different confining pressures

σ_3 (MPa)	E_{50} (GPa)	E_S (GPa)	$\varepsilon_{1c} (\times 10^{-3})$	σ_{cr} (MPa)	σ_{sr} (MPa)	σ_P (MPa)	σ_S (MPa)
0 (A3 [#])	28.47	46.50	3.957	7.57	7.57	96.37	96.37
0 (A4 [#])	30.15	43.61	2.845	6.30	6.30	99.11	99.11
5	32.46	36.36	3.822	35.57	40.57	98.56	103.56
10	38.63	42.34	4.108	64.11	74.11	112.54	122.54
20	44.47	46.08	8.267	95.77	115.77	126.28	146.28
30	46.41	46.53	19.30	128.51	158.51	144.84	174.84
40	46.76	48.08	23.45	157.36	197.36	167.92	207.92
50	51.75	53.07	20.64	183.89	233.89	185.71	235.71

$$\sigma_{sr} = \sigma_{cr} + \sigma_3; \sigma_S = \sigma_P + \sigma_3$$

Fig. 6 Influence of the confining pressure on the Young’s modulus and peak axial strain of marble

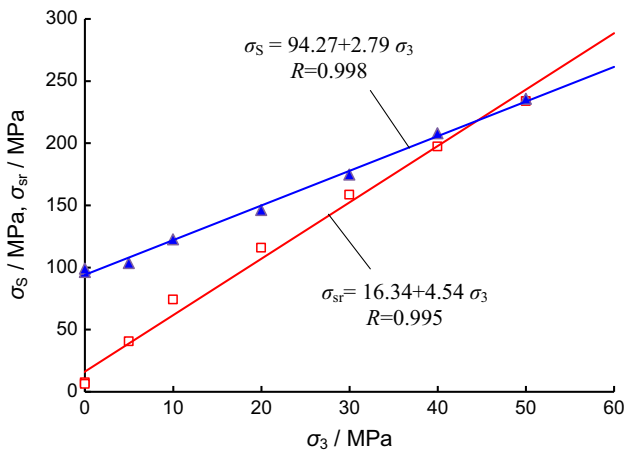
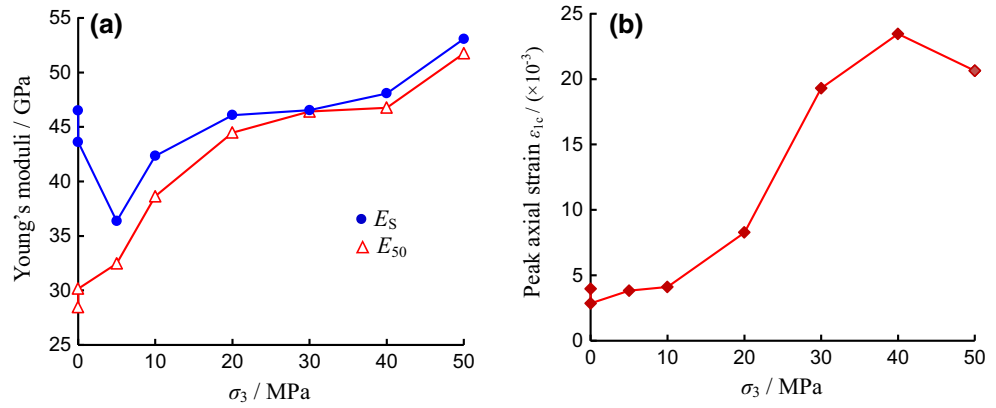


Fig. 7 Comparison of the peak and residual strength and crack damage threshold of marble. The *symbols* represent the experimental results, and the *lines* represent the theoretical values following the Mohr–Coulomb or Hoek–Brown criteria (*R* is the correlation coefficient of determination of the regression)

number generally have a higher attenuation of X-rays. The X-ray projection data from various directions are obtained by rotating the specimen 360°, as shown in Fig. 8a. We collected two-dimensional images at intervals of 0.18°, and thus, 2000 slice images were collected per specimen. A two-dimensional image representing the linear distribution of the X-ray attenuation was reconstructed using Fourier transformation of the projection data. A 3D data set of the specimen was obtained by stacking consecutive two-dimensional images.

The CT images were obtained from the center portion (a 50 mm diameter and 68 mm long) of each specimen, as shown in Fig. 8b, c. The slice images of the horizontal

cross-section shown in Fig. 9a were captured at 0.03 mm intervals. Therefore, a total of 2266 horizontal slices were obtained during the X-ray micro-CT testing of each marble specimen along the specimen axis. For the vertical cross-section shown in Fig. 9b, the slice images were captured at 0.5 mm intervals and the scanning sequence was from front to back. The horizontal and vertical slice images can be used to explore the internal damage in the marble material. In Fig. 9, *z* and *x* represent the height and the depth, respectively. Each horizontal CT slice image was divided into 1730 × 1730 pixels, and the spatial voxel resolution was approximately 0.03 mm.

Figure 10 illustrates the ultimate failure mode of the marble specimen under different confining pressures. From Fig. 10, the ultimate failure mode of marble specimens is very approximate and took on the shear fracture characteristics, which does not change with the confining pressure. Therefore, in this research, we use CT images of marble specimens tested at $\sigma_3 = 0$ (uniaxial compression) and 10 MPa to explore the internal damage mechanism. Figure 11 shows the comparison of the X-ray CT scanning surface images and the actual surface crack photographs of marble specimens after uniaxial and triaxial compression failure, where the black regions represent cracks or surface spalling, and other regions indicate no surface failure.

In Fig. 11, the X-ray CT scanning surface images approximate the actual surface crack photographs, which demonstrate that X-ray micro-CT scanning can be used to explore the internal damage in marble materials. To explore the extent of internal damage in specimens after uniaxial and triaxial compression failure, Figs. 12 and 13 show vertical cross-sections with different depths of marble specimens after uniaxial and triaxial compression failure

Table 2 Strength parameters of marble by the linear Mohr–Coulomb criterion

Different regression analysis	σ_0 (MPa)	<i>q</i>	<i>C</i> (MPa)	ϕ (°)	<i>R</i>
Using peak strength (σ_s)	94.27	2.79	28.22	28.2	0.998
Using residual strength (σ_{sr})	16.34	4.54	3.83	39.7	0.995

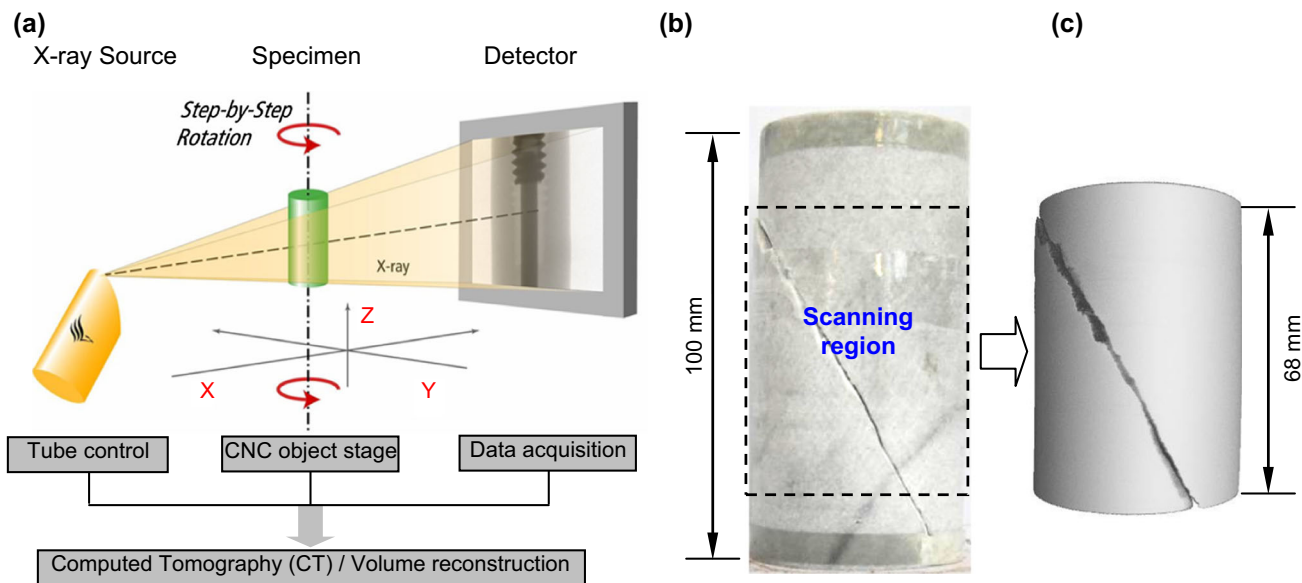


Fig. 8 Principle of the X-ray micro-CT observation and illustration of the scanning region. **a** The principle of X-ray CT observation and **b** experimental specimen

Fig. 9 Illustration of the scanning direction on the vertical (a) and horizontal (b) cross-section

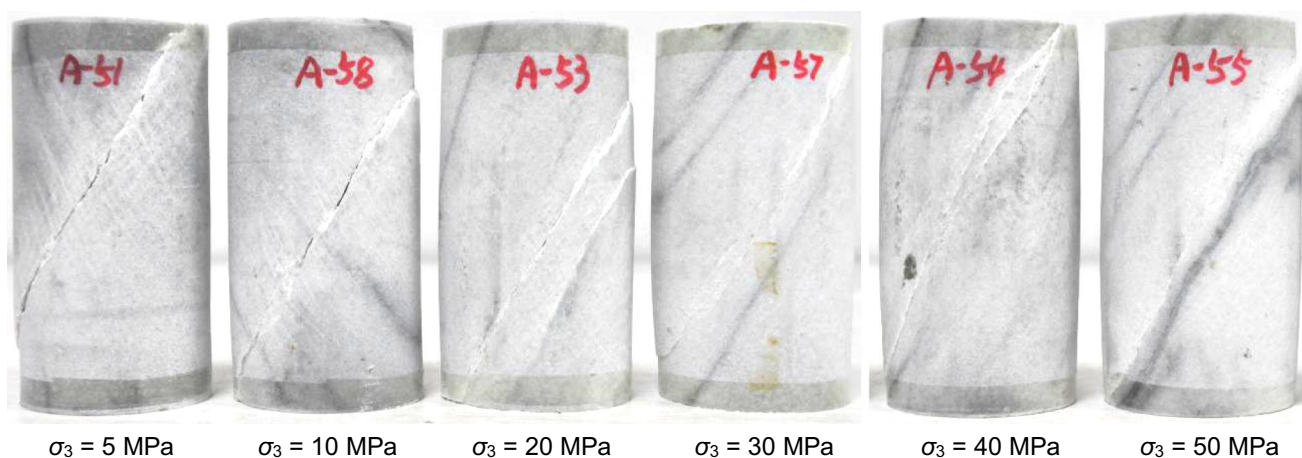
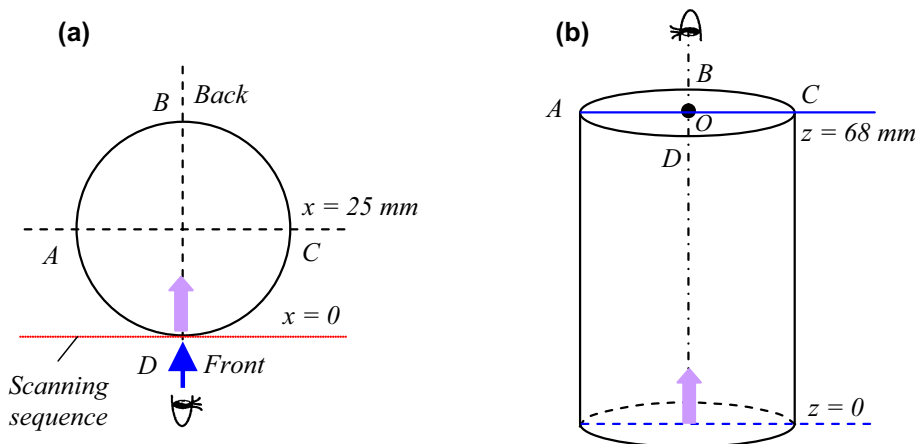


Fig. 10 Ultimate failure mode of marble specimen under different confining pressures

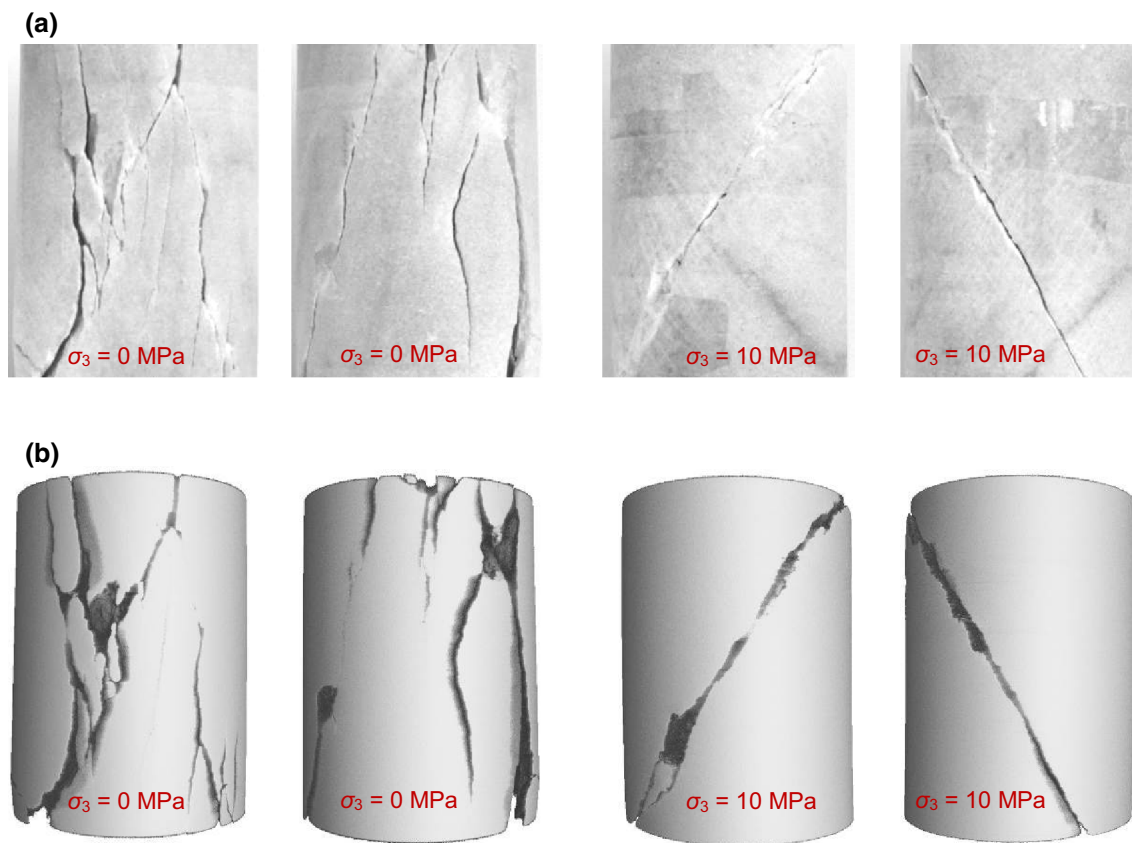


Fig. 11 Comparison of the X-ray CT scanning surface images (b) and actual surface crack photographs (a) of marble specimens after uniaxial ($\sigma_3 = 0$ MPa) and triaxial compression failure ($\sigma_3 = 10$ MPa)

($\sigma_3 = 10$ MPa), respectively. Generally, as shown in Figs. 12 and 13, the system of cracks under triaxial conditions is less complicated than that under uniaxial conditions, which also agrees well with the findings from the macro-CT (the resolution was approximately 0.3–1.0 mm) observations of faulting in the Westerly granite under uniaxial and triaxial conditions (Kawakata et al. 1999). Furthermore, the fracture planes under triaxial compression have lower angles (the angle that between the normal to crack plane and the maximum principal stress) than under uniaxial compression.

Figure 14 shows 3D CT images of failed marble specimens. In the 3D images, the fracture regions are black, and the other regions are transparent. From Fig. 14, the marble specimen under uniaxial compression has a typical axial splitting failure mode, which is also identical to the surface fracture shown in Fig. 11 and the vertical cross-sections shown in Fig. 12. However, the failure mode of the marble specimen after triaxial compression failure is different to that after uniaxial compression failure. At a confining pressure of 10 MPa, the specimen shows a single shear failure mode. By rotating the image of the specimen, the trace of the shear fracture appears as an approximate plane,

which indicates that the dip is more uniform throughout the shear fracture curve. The single shear fracture curve under a confining pressure of 10 MPa is also demonstrated by the surface fracture shown in Fig. 11 and vertical cross-sections shown in Fig. 12. The axial splitting tensile fracture and shear fracture of the marble specimen under uniaxial and triaxial compression can be further inferred from microscopic observations on the fracture surface of the failed specimen, as shown in Fig. 15. The shear slippage surface is very smooth, but the tensile fracture surface is very rough.

5 Discussion

Figures 16 and 17 show horizontal cross-sections with different heights of marble specimens after uniaxial compression failure and triaxial compression failure at $\sigma_3 = 10$ MPa, respectively. From Fig. 16, we can analyze the effect of the height (z) on the extent of the internal damage to the marble material after uniaxial compression failure. At $z = 5$ –20 mm, the horizontal cross-section is located in the bottom region of the specimen and a number

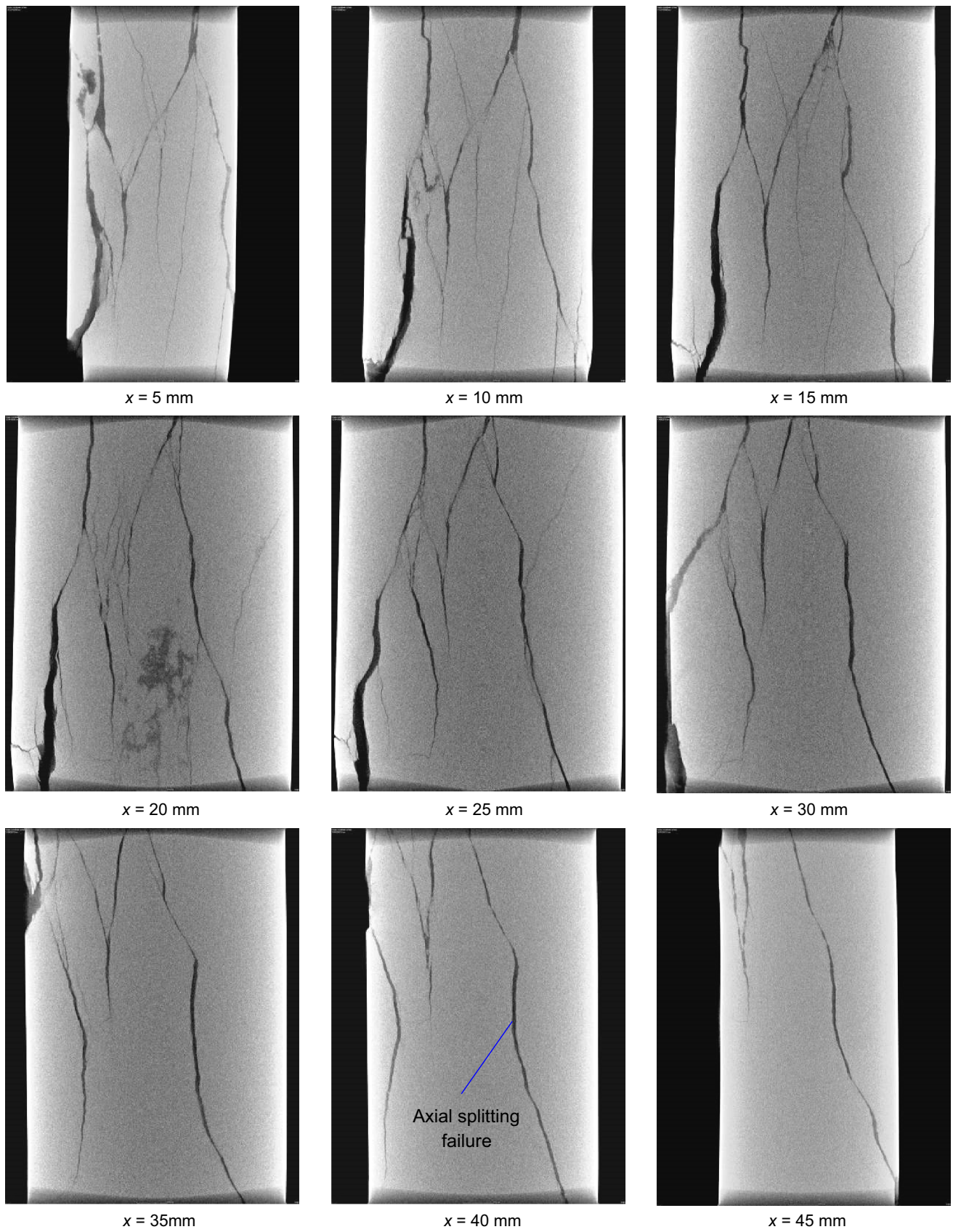


Fig. 12 Vertical cross-sections with different depths of marble specimen after uniaxial compression failure

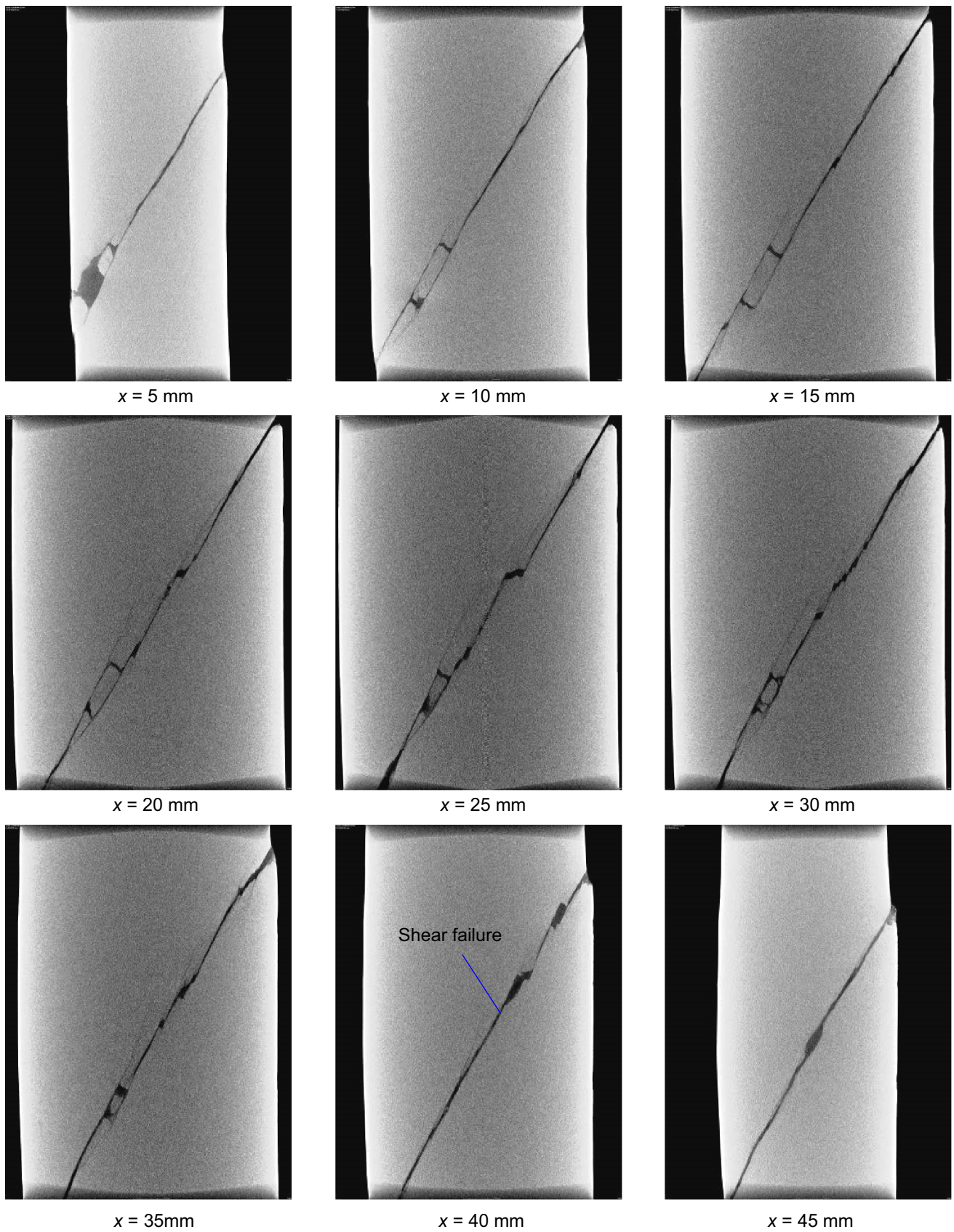


Fig. 13 Vertical cross-sections with different depths of marble specimen after triaxial compression failure ($\sigma_3 = 10$ MPa)

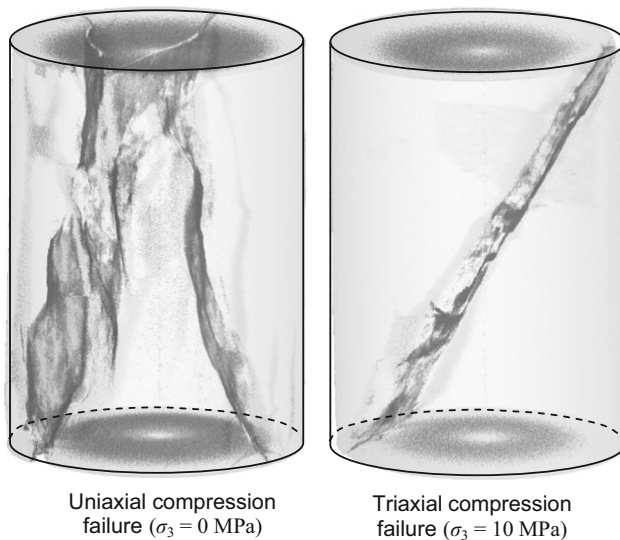


Fig. 14 Three-dimensional CT images of failed marble specimen

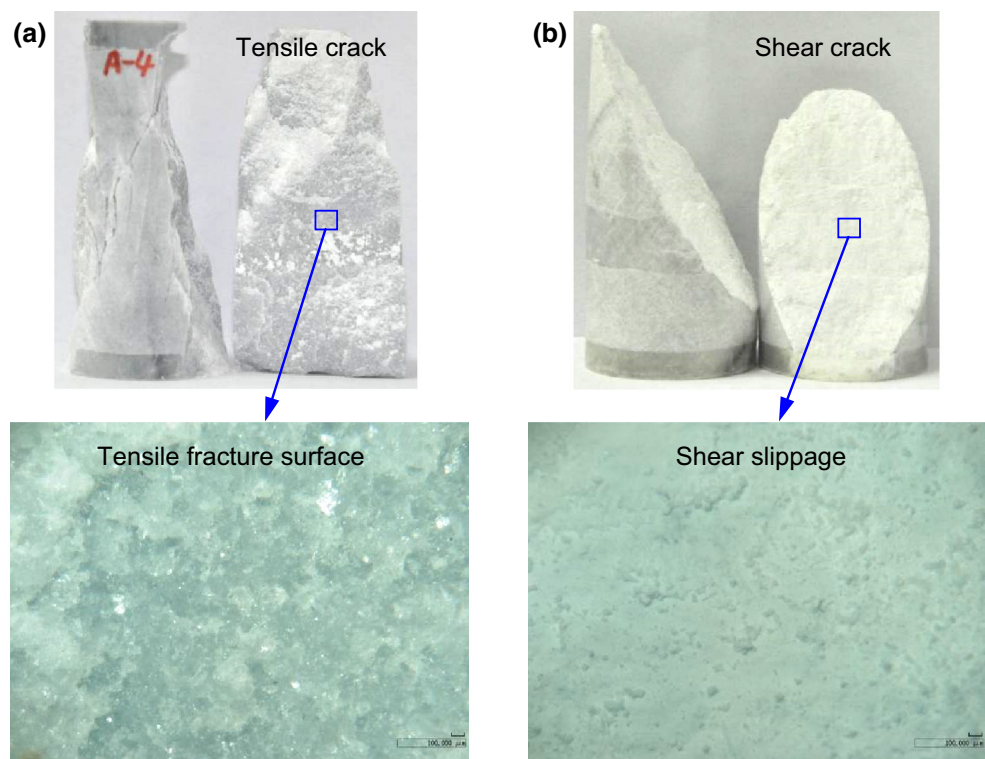
of cracks are observed, but the system of cracks is very simple, which can also be demonstrated from the bottom region shown in Fig. 14. Moreover, the width and length of these cracks are different, indicating various damage extents in the same cross-section. At $z = 20\text{--}50$ mm, the internal damage to the specimen is more serious. Many cracks are observed, and the system of cracks is very complex, which results from crack propagation and

coalescence inside the specimen with the increase in deformation. However, at $z = 50\text{--}60$ mm, the crack system becomes more simple compared with that at $z = 20\text{--}50$ mm. The above statement suggests that the cracks are first initiated in the center of the specimen and then propagate toward the top and bottom regions of the specimen. In addition, with the increase in height, the width of crack 1 first decreases and then increases, and the path of crack 1 is not a line but a curve. Crack 2 moves from the right side to the central region, and the length of crack 3 decreases gradually with the increase in height. The angle between crack 4 and the horizontal direction decreases with the increase in height.

From Fig. 17, one main crack cuts through the cylindrical specimen. At $z = 5\text{--}10$ and $20\text{--}60$ mm, only one main crack is observed, whereas at $z = 10\text{--}20$ mm, two cracks were observed. With the increase in height, the main crack moves toward the right side from the left side. The main crack is approximately linear, which also indicates that the shear fracture is an approximate plane. The above statement may indicate that cracks first initiate from the bottom or the top boundary of the specimen and then propagate toward the central region of the specimen.

To quantitatively evaluate the fracture extent of the internal damage of the marble specimen after uniaxial and triaxial compression failure, each horizontal CT image, as shown in Figs. 16 and 17, was processed using Matlab software (Gui et al. 2012; Yang et al. 2015b) and changed

Fig. 15 Microscopic observations of the fracture surface of marble specimens under uniaxial and triaxial compression. **a** Tensile fracture surface represents the tensile crack, uniaxial compression failure ($\sigma_3 = 0$ MPa) and **b** shear slippage indicates the shear crack, triaxial compression failure ($\sigma_3 = 10$ MPa)



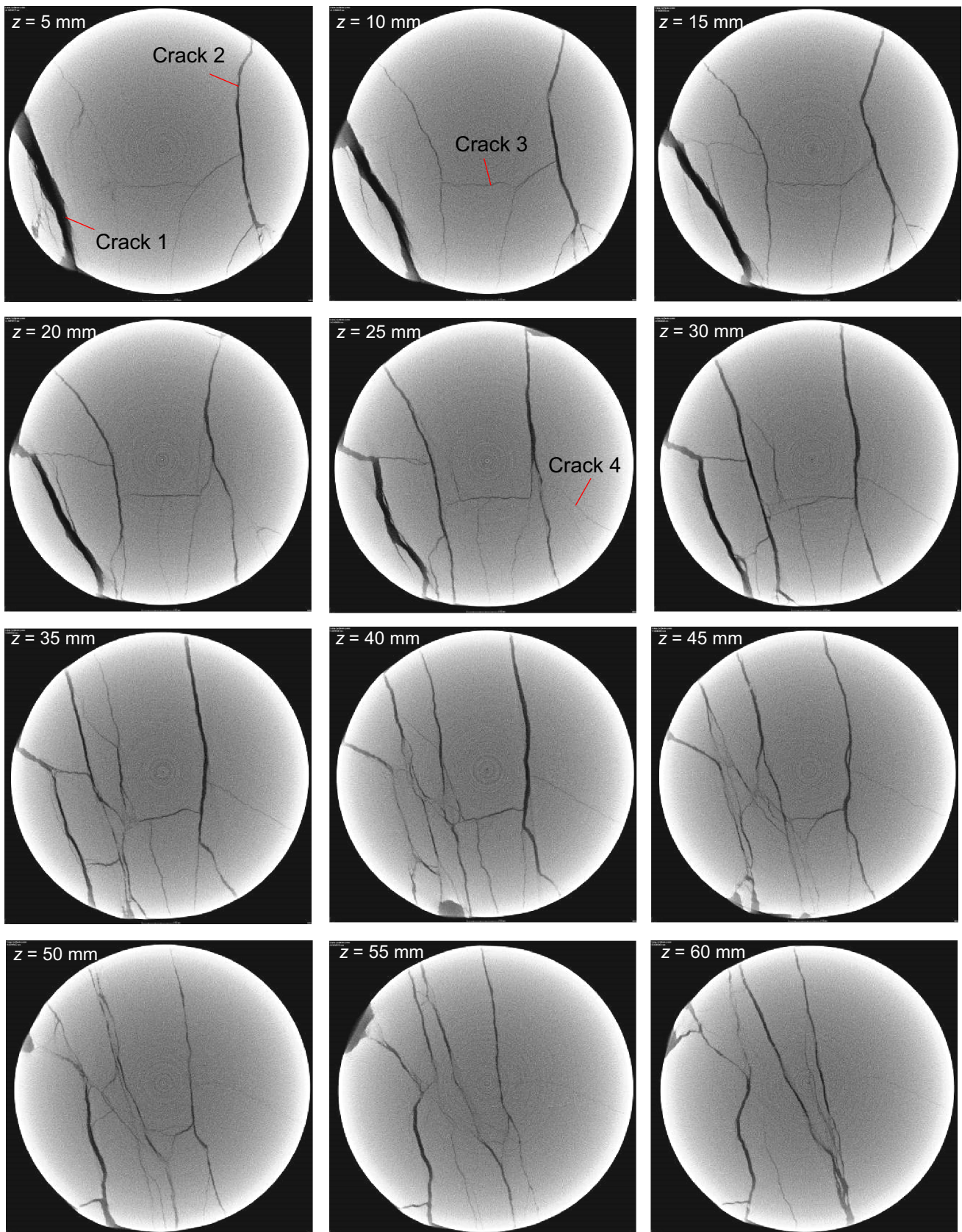


Fig. 16 Horizontal cross-sections with different heights of marble specimen after uniaxial compression failure

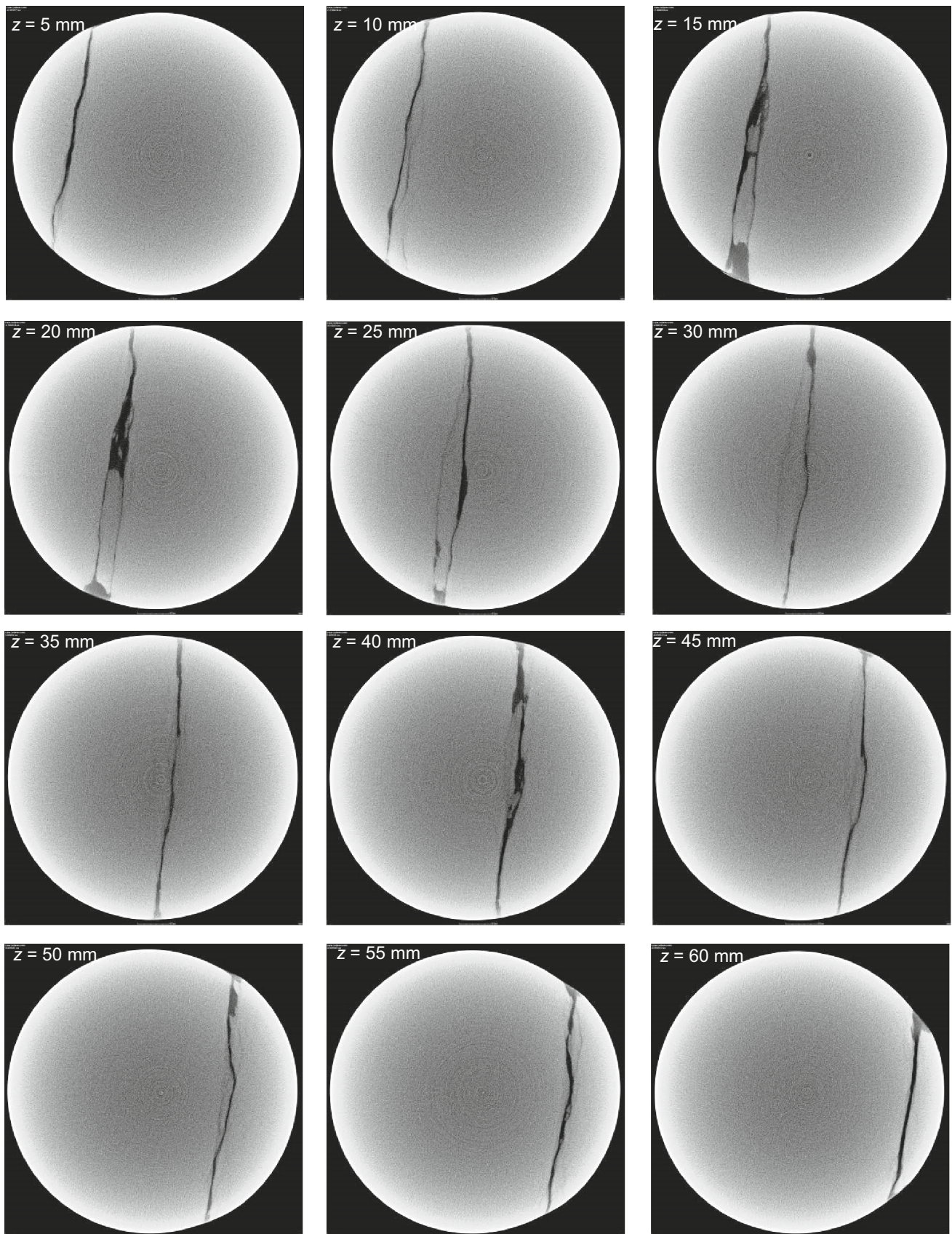


Fig. 17 Horizontal cross-sections with different heights of marble specimen after uniaxial compression failure ($\sigma_3 = 10$ MPa)

to binarized pictures (Fig. 18). In Fig. 18, the white regions represent the cracks, whereas the black regions represent intact rocks that did not experience any failure. Generally, the crack system shown in Fig. 18 agrees well with the experimental results shown in Figs. 16 and 17. Based on the binarized pictures for all horizontal cross-sections after uniaxial and triaxial compression failure, we determined the crack area and aperture extent (i.e., the percentage ratio of the crack area to the entire area) for each horizontal cross-section. Thus, we were able to quantitatively investigate the effect of height (z) on the extent of the internal damage of the marble material.

Figure 19 shows the evolution of crack area and aperture extent along different heights (z) after uniaxial and triaxial compression failure ($\sigma_3 = 10$ MPa). From Fig. 19a, the crack area after uniaxial compression failure increases from 88.88 mm^2 at $z = 5$ – 102.02 mm^2 at $z = 15$ mm, and then decreases to 93.02 mm^2 at $z = 20$ mm. Second, the crack area increases to 111.4 mm^2 at $z = 30$ mm. Then, the crack area decreases from 111.4 mm^2 at $z = 30$ – 46.86 mm^2 at $z = 50$ mm. Finally, the crack area increases to 86.64 mm^2 at $z = 60$ mm. However, after triaxial compression failure

($\sigma_3 = 10$ MPa), the crack area increases gradually from 20.91 mm^2 at $z = 5$ – 65.74 mm^2 at $z = 15$ mm and then decreases to 29.77 mm^2 at $z = 35$ mm. Then, the crack area obviously increases to 51.09 mm^2 at $z = 40$ mm. In the end, the crack area of marble specimens tends to a stable value with the increase in height. From Fig. 19b, we can see that the evolution of the aperture extent approximates to that of the crack area. Figure 20 illustrates the relationship between crack area and aperture extent along different heights (z) of marble specimen after uniaxial and triaxial compression failure ($\sigma_3 = 10$ MPa). From Fig. 20, it can be seen that the crack area has a good linear relationship with the aperture extent along different heights (z), which does not depend on the confining pressure.

To analyze the brittle–ductile transition mechanism of the marble specimen shown in Fig. 5, conceptual failure models (see Figs. 21, 22) of the marble material under uniaxial and triaxial compression were proposed in this research. In Figs. 21 and 22, σ_a , σ_p , σ_b and σ_{cr} represent the yielding stress, peak strength, post-peak drop stress and residual strength, respectively. Marble is very homogeneous at the macroscopic scale, but strongly heterogeneous at the mesoscopic scale. The macroscopic fracture

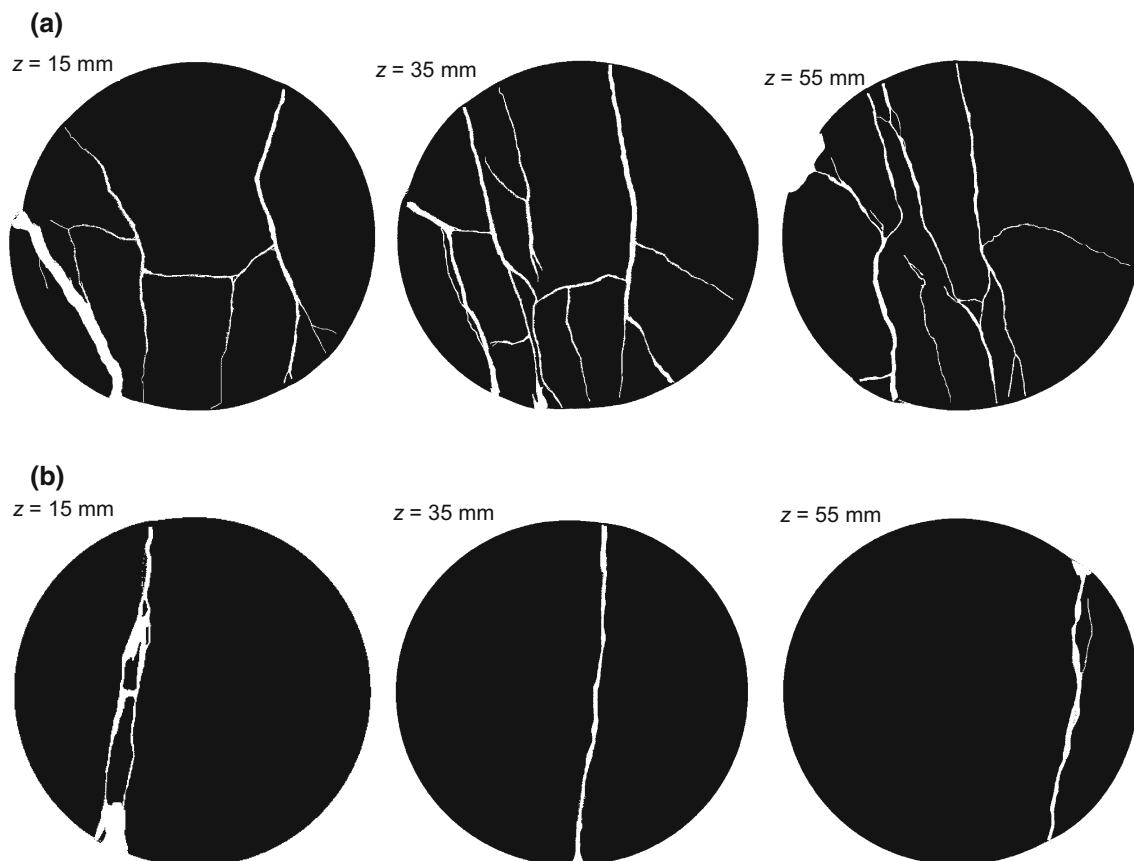


Fig. 18 Typical binarized pictures of horizontal cross-sections of marble specimen after uniaxial compression (a) and triaxial compression failure ($\sigma_3 = 10$ MPa) (b)

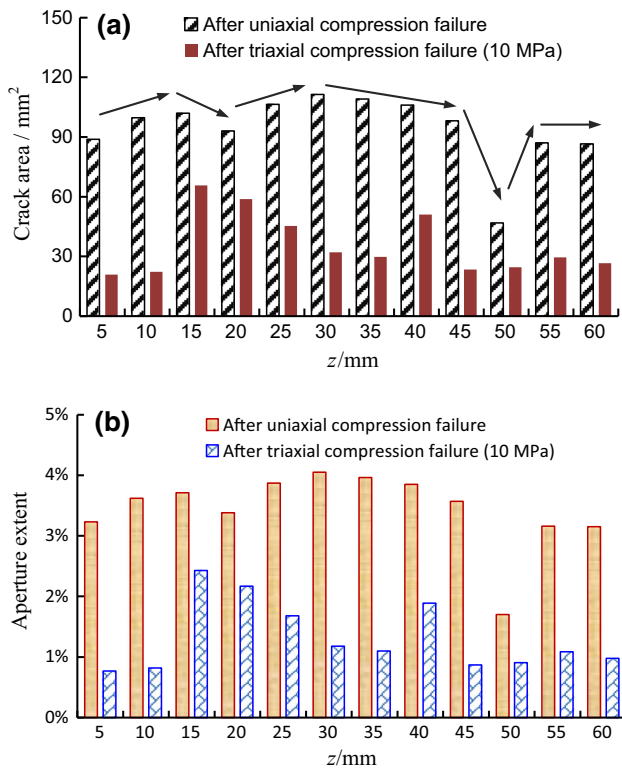


Fig. 19 Evolution of the crack area and aperture extent along different heights (z) of marble specimen after uniaxial and triaxial compression failure ($\sigma_3 = 10$ MPa)

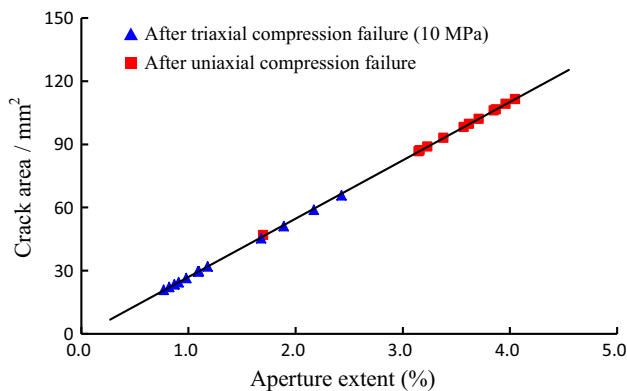


Fig. 20 Relation between crack area and aperture extent along different heights (z) of marble specimen after uniaxial and triaxial compression failure ($\sigma_3 = 10$ MPa)

phenomenon may be regarded as the average effect of the mesoscopic failure and the heterogeneous mesoscopic failure can be described by a probability and statistics theory, such as the Weibull distribution. Thus, we propose that mesoscopic element material can be regarded as a random variable and distributes randomly in the rock specimen. The strength and stiffness of the mesoscopic element material in the specimen varies strongly from one element to another.

Under uniaxial compression, the marble specimen is loaded to σ_a with increasing axial deformation and the tensile cracks initiate from the tips of the fissures for larger fissure angles, whereas the tensile cracks initiate from a certain distance to the tips of the fissures for smaller fissure angles (Fig. 21a). At this time, a small part of the mesoscopic material elements with low strength and stiffness first reaches their maximum supporting capacity and produces plastic deformation during the yielding of specimen. Afterward, when the specimen is loaded to peak strength (σ_p), tensile cracks begin to propagate (Fig. 21b) in a direction that is approximately parallel to the axial stress, e.g., wing cracks. However, after the macroscopic stress–strain response of the tested marble specimen reaches peak stress, the mesoscopic material elements with high strength and stiffness will unload because they did not reach their maximum supporting limit, and plastic deformation in the specimen is not uniform. Therefore, following a decrease in the macroscopic axial deviatoric stress, the plastic deformation that is initiated will further concentrate on those failed mesoscopic material elements with low strength and stiffness, which results in localized deformation. Thus, specimens under lower confining pressures have a softening behavior (Fig. 21c). During deformation, some tensile cracks coalesce. When the specimen reaches the residual stress (σ_{cr}), some axial splitting tensile fractures are observed (Fig. 21d).

When the marble specimen is loaded to σ_a under confining pressure with the increase in axial deformation, the cracks are initiated from the tips of fissures (Fig. 22a). Most of the mesoscopic material elements with low strength and stiffness first reach their maximum supporting capacity, yield softening and produce the plastic deformation. Then, the axial stress must be increased continuously to allow the specimen to fail macroscopically. When the specimen is loaded to peak strength (σ_p), the cracks begin to propagate (Fig. 22b). The direction of crack propagation is different under uniaxial compression, and the cracks will propagate toward the left and right boundaries of the specimen. At this time, the mesoscopic material elements with higher strength and stiffness in the specimen will also reach their maximum supporting limit, yielding failure and initiating plastic deformation. Therefore, the total deformation in the specimen tends to uniform and the plastic deformation of the specimen will increase, which results in a distinct yielding platform in the macroscopic stress–strain curves close to the peak stress. Furthermore, the yielding platform of the specimen with higher confining pressures is more obvious. When the stress is loaded to post-peak drop stress (σ_c), the specimen will form the shear fracture due to the crack coalescence (Fig. 22c). When the specimen reaches the

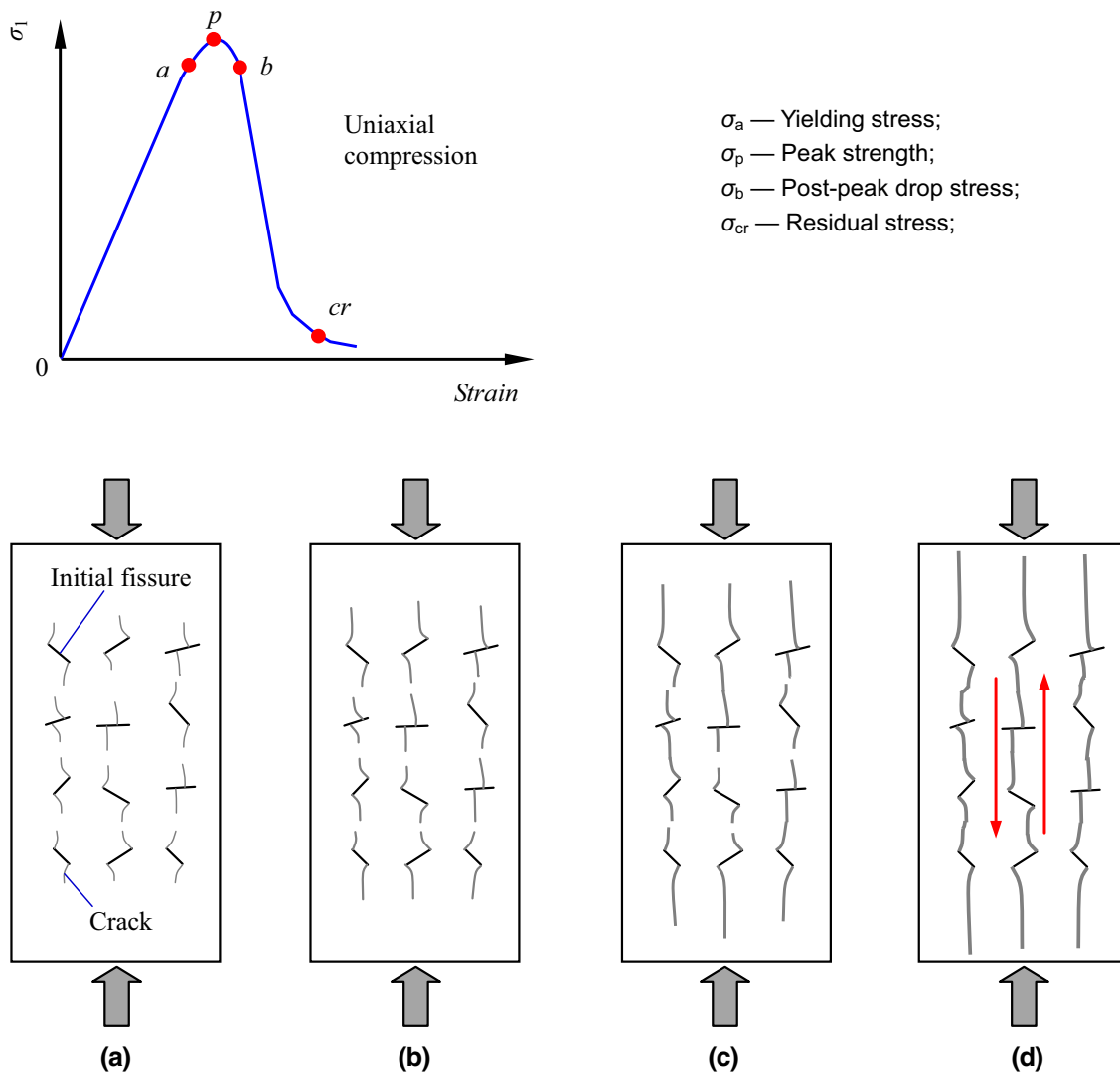


Fig. 21 Conceptual model of marble material under uniaxial compression: Axial splitting tensile fracture is due to the coalescence of wing cracks starting from preexisting fissures

residual stress (σ_{cr}), the shear friction slippage will control the axial capacity (Fig. 22d).

6 Conclusions

1. The Young's modulus of deeply buried marble increased nonlinearly with increasing confining pressure. The difference between the elastic modulus and the deformation modulus tended to decrease as the confining pressure increased, which was the result of the more pronounced stage of micro-crack closure at lower confining pressures. The peak and residual strengths of marble exhibited a clear linear relationship with the confining pressure, which can be best described by the linear Mohr–Coulomb criterion. The

2. After uniaxial and triaxial compression failure, the marble specimens were analyzed using an X-ray micro-CT scanning system. Many X-ray CT images of the specimens were generated, and 3D images of the specimens were reconstructed. The surface X-ray CT scanning surface images of the marble specimens were in good agreement with the actual surface crack photographs, which demonstrates that X-ray micro-CT scanning can be used to explore the damage of rock material. To quantitatively evaluate the effect of the height on the extent of the internal damage of the marble specimen, the crack area and aperture extent

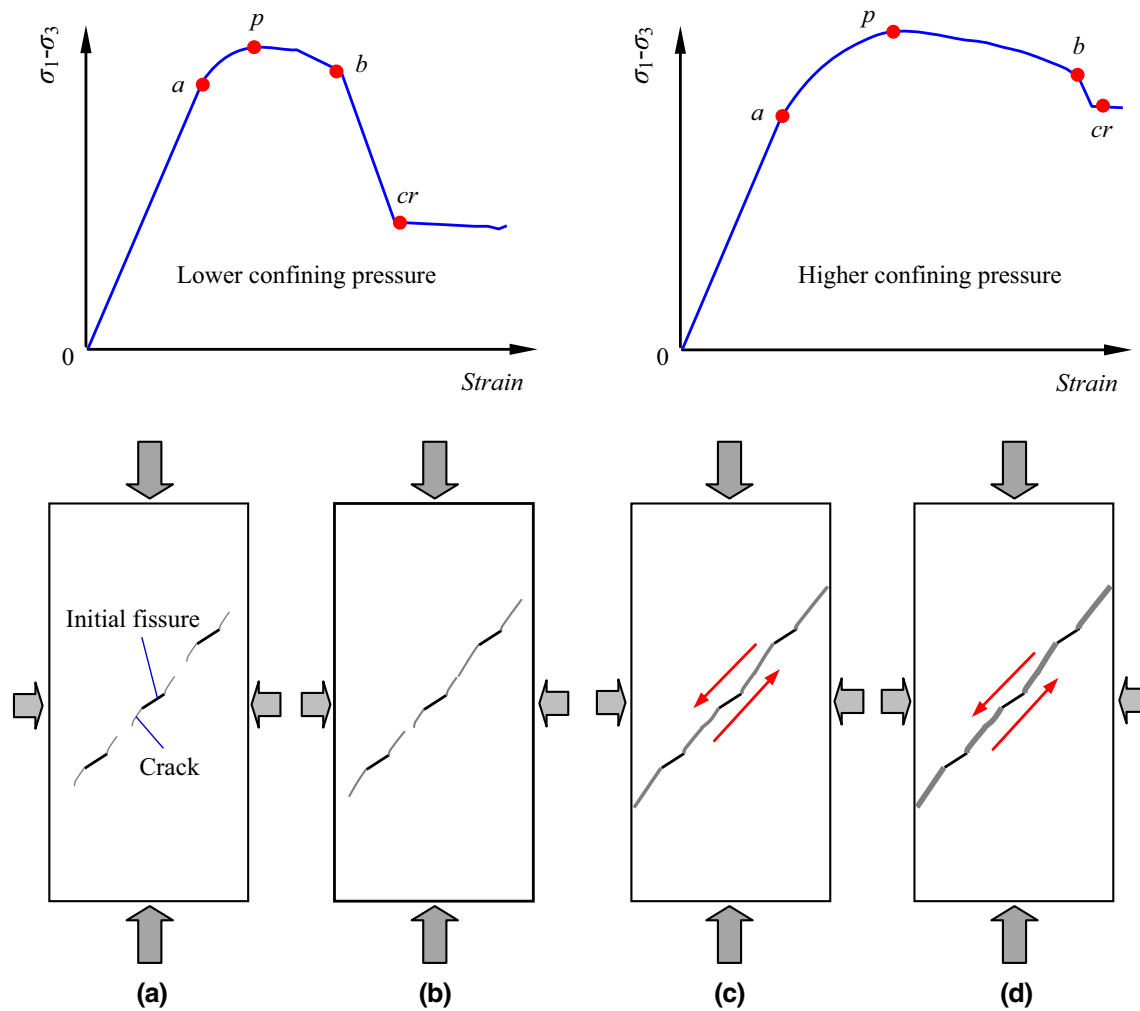


Fig. 22 Conceptual model of marble material under different confining pressures: single shear fracture

for each horizontal cross-section were calculated by analyzing the binarized pictures and indicated that height had a distinct influence on the crack area or aperture extent.

- Under uniaxial compression, marble specimens were dominated by axial splitting tensile cracks. However, under different confining pressures, marble specimens were dominated by a single shear crack. Based on the horizontal and vertical cross-sections of marble specimens, the system of crack planes under uniaxial compression was more complicated than that under triaxial compression, which also agrees well with the crack area and aperture extent with respect to the confining pressure. Finally, the brittle–ductile transition mechanism of marble was discussed and interpreted according to the proposed conceptual models.

Acknowledgments This research was supported by the Fundamental Research Funds for the Central Universities (2015XKZD05). The authors would like to express their sincere gratitude to the editor,

Giovani Barla, and two anonymous reviewers for their valuable comments, which have greatly improved this paper.

References

- Akbardoost J, Ayatollahi MR (2014) Experimental analysis of mixed mode crack propagation in brittle rocks: the effect of non-singular terms. *Eng Fract Mech* 129:77–89
- Aliha MRM (2014) Indirect tensile test assessments for rock materials using 3-D disc-type specimens. *Arab J Geosci* 7(11):4757–4766
- Aliha MRM, Ayatollahi MR, Akbardoost J (2012) Typical upper bound–lower bound mixed mode fracture resistance envelopes for rock material. *Rock Mech Rock Eng* 45(1):65–74
- Aliha MRM, Hosseinpour GR, Ayatollahi MR (2013) Application of cracked triangular specimen subjected to three-point bending for investigating fracture behavior of rock materials. *Rock Mech Rock Eng* 46(5):1023–1034
- Ayatollahi MR, Aliha MRM (2007) Fracture toughness study for a brittle rock subjected to mixed mode I/II loading. *Int J Rock Mech Min Sci* 44:617–624
- Chang SH, Lee CI, Jeon S (2002) Measurement of rock fracture toughness under modes I and II and mixed-mode conditions by using disc-type specimens. *Eng Geol* 66:79–97

- Fairhurst CE, Hudson JA (1999) Draft ISRM suggested method for the complete stress–strain curve for the intact rock in uniaxial compression. *Int J Rock Mech Min Sci* 36(3):279–289
- Feng XT, Chen SL, Zhou H (2004) Real-time computerized tomography (CT) experiments on sandstone damage evolution during triaxial compression with chemical corrosion. *Int J Rock Mech Min Sci* 41(2):181–192
- Feng GL, Feng XT, Chen BR, Xiao YX (2015) Microseismic sequences associated with rockbursts in the tunnels of the Jinping II hydropower station. *Int J Rock Mech Min Sci* 80:89–100
- Funatsu T, Kuruppu M, Matsui K (2014) Effects of temperature and confining pressure on mixed-mode (I–II) and mode II fracture toughness of Kimachi sandstone. *Int J Rock Mech Min Sci* 67:1–8
- Ge XR, Ren JX, Pu YB, Ma W, Zhu YL (2001) Real-in time CT test of the rock meso-damage propagation law. *Sci China (Ser E)* 44(3):328–336
- Gui YL, Zhao GF, Khalili N (2012) Experimental investigation of desiccation of clayey soils. In: 22th Australasian conference on the mechanics of structure and materials (ASMSM22), 11–14 Dec, Sydney, Australia
- Hirono T, Takahashi M, Nakashima S (2003) In situ visualization of fluid flow image within deformed rock by X-ray CT. *Eng Geol* 70:37–46
- Hirono T, Sakaguchi M, Otsuki K, Sone H, Fujimoto K, Mishima T, Lin W, Tanikawa W, Tanimizu M, Soh W, Yeh EC, Song SR (2008) Characterization of slip zone associated with the 1999 Taiwan Chi-Chi earthquake: X-ray CT image analyses and microstructural observations of the Taiwan Chelungpu fault. *Tectonophysics* 449:63–84
- Huang D, Li YR (2014) Conversion of strain energy in triaxial unloading tests on marble. *Int J Rock Mech Min Sci* 66:160–168
- Jaeger JC, Cook NGW, Zimmerman RW (2007) *Fundamentals of rock mechanics*, 4th edn. Blackwell Publishing, Oxford
- Jiang Q, Feng XT, Xiang TB, Su GS (2010) Rockburst characteristics and numerical simulation based on a new energy index: a case study of a tunnel at 2500 m depth. *Bull Eng Geol Environ* 69:381–388
- Kawakata H, Cho A, Kiyama T, Yanagidani T, Kusunose K, Shimada M (1999) Three-dimensional observations of faulting process in Westerly granite under uniaxial and triaxial conditions by X-ray CT scan. *Tectonophysics* 313:293–305
- Li SJ, Feng XT, Li ZH (2012a) Evolution of fractures in the excavation damaged zone of a deeply buried tunnel during TBM construction. *Int J Rock Mech Min Sci* 55(10):125–138
- Li SJ, Feng XT, Li ZH, Chen BR, Zhang CQ, Zhou H (2012b) In situ monitoring of rockburst nucleation and evolution in the deeply buried tunnels of Jinping II hydropower station. *Eng Geol* 137(138):85–96
- Li XP, Zhao H, Wang B, Xiao TL (2013) Mechanical properties of deep-buried marble material under loading and unloading tests. *J Wuhan Univ Technol Mater* 28(3):514–520
- Meier T, Rybacki E, Backers T, Dresen G (2014) Influence of bedding angle on borehole stability: a laboratory investigation of transverse isotropic oil shale. *Rock Mech Rock Eng*. doi:10.1007/s00603-014-0654-1
- Qiu SL, Feng XT, Xiao JQ, Zhang CQ (2014) An experimental study on the pre-peak unloading damage evolution of marble. *Rock Mech Rock Eng* 47:401–409
- Sufian A, Russell AR (2013) Microstructural pore changes and energy dissipation in Gosford sandstone during pre-failure loading using X-ray CT. *Int J Rock Mech Min Sci* 57:119–131
- Wu SY, Shen MB, Wang J (2010) Jinping hydropower project: main technical issues on engineering geology and rock mass. *Bull Eng Geol Environ* 69:325–332
- Yang SQ, Jiang YZ, Xu WY, Chen XQ (2008) Experimental investigation on strength and failure behavior of pre-cracked marble under conventional triaxial compression. *Int J Solids Struct* 45:4796–4819
- Yang SQ, Dai YH, Han LJ, Jin ZQ (2009) Experimental study on mechanical behavior of brittle marble samples containing different flaws under uniaxial compression. *Eng Fract Mech* 76:1833–1845
- Yang SQ, Xu P, Ranjith PG, Chen GF, Jing HW (2015a) Evaluation of creep mechanical behavior of deep-buried marble under triaxial cyclic loading. *Arab J Geosci* 8:6567–6582
- Yang SQ, Ranjith PG, Huang YH, Yin PF, Jing HW, Gui YL, Yu QL (2015b) Experimental investigation on mechanical damage characteristics of sandstone under triaxial cyclic loading. *Geophys J Int* 201:662–682
- Zhao GF, Russell AR, Zhao XB, Khalili N (2014) Strain rate dependency of uniaxial tensile strength in Gosford sandstone by the Distinct Lattice Spring Model with X-ray micro CT. *Int J Solids Struct* 51:1587–1600